

Layered $\text{Li}_{1+x}(\text{Ni}_{0.425}\text{Mn}_{0.425}\text{Co}_{0.15})_{1-x}\text{O}_2$ Positive Electrode Materials for Lithium-Ion Batteries

Nicolas Tran, Laurence Croguennec, Christine Labrugère, C. Jordy, Ph. Biensan, Claude Delmas

Abstract :

Layered $\text{Li}_{1+x}(\text{Ni}_{0.425}\text{Mn}_{0.425}\text{Co}_{0.15})_{1-x}\text{O}_2$ materials ($0 \leq x \leq 0.12$) were prepared at 1000°C for 12 h in air by a coprecipitation method. As x increased in $\text{Li}_{1+x}(\text{Ni}_{0.425}\text{Mn}_{0.425}\text{Co}_{0.15})_{1-x}\text{O}_2$, the substitution of x Li^+ ions for x transition metal ions induced for charge compensation an increase in the average transition metal oxidation state. X-ray photoelectron spectroscopy analyses showed that cobalt and manganese were present in these materials in the trivalent and tetravalent states, respectively, and that increasing overlithiation led to the oxidation of Ni^{2+} ions into Ni^{3+} ions. The refinement of the crystal structure of these materials in the $R\bar{3}m$ space group and magnetic measurements showed a decrease in the Ni occupancy in the Li layers with increasing overlithiation. From an electrochemical point of view, the reversible capacity in the 2–4.3 V range decreased with overlithiation

Keywords :

Although LiCoO_2 is suitable for the lithium-ion battery application, its high cost and toxicity prevent its use in low-price or large devices. Positive electrodes with LiNiO_2 revealed an attractive reversible capacity¹ but suffered from a quite poor capacity retention² and also from a low thermal stability of their deintercalated phases.^{3,4,5,6} Partial substitution for nickel allowed an optimization of these properties for compositions such as $\text{LiNi}_{(1-x-y)}\text{Co}_x\text{Al}_y\text{O}_2$.^{7,8,9} Nevertheless, there is still a need for cheaper and safer positive electrode materials with higher electrochemical performances. Recently lithium-rich manganese-based materials such as $\text{Li}[\text{Ni}_x\text{Li}_{(1/3-2x/3)}\text{Mn}_{(2/3-x/3)}]\text{O}_2$ and $\text{Li}[\text{Co}_x\text{Li}_{(1/3-x/3)}\text{Mn}_{(2/3-2x/3)}]\text{O}_2$ were extensively studied by various research groups.^{10,11,12,13} Interesting results were obtained, for instance for the $\text{Li}[\text{Ni}_{1/3}\text{Li}_{1/9}\text{Mn}_{5/9}]\text{O}_2$ phase with a capacity of 230 mAh/g between 2.0 and 4.6 V at 55°C .¹⁴ In all these materials, the manganese ions are in the tetravalent state in the pristine material¹⁵ so that they are electrochemically inactive. Because there are no Mn^{3+} ions, no structural evolution to the spinel structure is expected to occur upon cycling, on the contrary to what was observed for the layered LiMnO_2 .^{16,17,18,19} Furthermore, the presence of a large amount of manganese ions at the stable tetravalent oxidation state is thought to be responsible for a higher thermal stability. Differential scanning calorimetry experiments (DSC) on charged electrodes of $\text{Li}[\text{Ni}_x\text{Li}_{(1/3-2x/3)}\text{Mn}_{(2/3-x/3)}]\text{O}_2$ for $x=5/12$ indicate that this material should be thermally safer than LiCoO_2 .¹⁰ The DSC profiles of the fully oxidized $\text{Li}_x[\text{Li}_{0.12}\text{Ni}_z\text{Mg}_{0.32-z}\text{Mn}_{0.56}]\text{O}_2$ ($z=0.3$) material also demonstrate much higher thermal stability than Li_xCoO_2 .²⁰ Note also that most of these overlithiated materials exhibit an irreversible plateau at around 4.5 V/Li during the first charge. The origin of this plateau was attributed by Lu and Dahn to be due to an irreversible oxygen loss.¹⁴

Ever since $\text{LiNi}_{1/3}\text{Mn}_{1/3}\text{Co}_{1/3}\text{O}_2$ material was shown by Ohzuku *et al.* to deliver a high discharge capacity close to 200 mAh/g,²¹ a lot of research in the lithium-ion battery field has focused on the layered $\text{Li}(\text{Ni},\text{Mn},\text{Co})\text{O}_2$ materials.^{22,23,24} In a previous paper we discussed the synthesis conditions of the $\text{LiNi}_{0.425}\text{Mn}_{0.425}\text{Co}_{0.15}\text{O}_2$ phases and their optimization from an electrochemical point of view.²⁴ In this paper, we report the structure and the electrochemical behavior of the $\text{Li}_{1+x}(\text{Ni}_{0.425}\text{Mn}_{0.425}\text{Co}_{0.15})_{1-x}\text{O}_2$ materials ($0 \leq x \leq 0.12$). The classical coprecipitation method was used for syntheses because it leads to the best electrochemical performance.²⁴ The relationships between the chemical composition, the physical properties, the structure, and the electrochemical performances are discussed in this paper.

Experimental

$\text{Ni}(\text{NO}_3)_2 \cdot 6\text{H}_2\text{O}$ (97% Prolabo), $\text{Mn}(\text{NO}_3)_2 \cdot 4\text{H}_2\text{O}$ (98% Fluka), $\text{Co}(\text{NO}_3)_2 \cdot 6\text{H}_2\text{O}$ (98% Prolabo), LiOH (98+% Alfa Aesar), and NH_4OH (28–30% J.T. Baker) were used as starting materials.

The $\text{Li}_{1+x}(\text{Ni}_{0.425}\text{Mn}_{0.425}\text{Co}_{0.15})_{1-x}\text{O}_2$ ($x_{\text{nom.}}=0, 0.03, 0.10, 0.20, 0.25, \text{ and } 0.33$, $x_{\text{nom.}}$ for nominal x value) materials were prepared using the coprecipitation method.²⁵ A mixed (1 M) aqueous solution of $\text{Ni}(\text{NO}_3)_2$, $\text{Mn}(\text{NO}_3)_2$, and $\text{Co}(\text{NO}_3)_2$ prepared with the 42.5/42.5/15 molar ratio was added dropwise through a buret into a basic solution [LiOH (1 M)/ NH_4OH (3 M)] under magnetic stirring. Note that the initial ratio $\text{Li}/(\text{Ni}+\text{Co}+\text{Mn})$ was adjusted in order to obtain the desired x value in $\text{Li}_{1+x}(\text{Ni}_{0.425}\text{Mn}_{0.425}\text{Co}_{0.15})_{1-x}\text{O}_2$. A green-brown mixed hydroxide was precipitated. Water was removed by evaporation at 80°C under primary vacuum using a rotavapor device. The resulting wet precipitate was dried overnight at 105°C , precalcined at 500°C for 5 h in air, and then calcined at 1000°C for 12 h in air in a tubular furnace. Heating speed was fixed to $5^\circ\text{C}/\text{min}$ and cooling speed was fixed to $4^\circ\text{C}/\text{min}$.

The materials were analyzed by X-ray diffraction (XRD) using a Siemens D5000 diffractometer equipped with a diffracted-beam monochromator (Cu $K\alpha$ radiation) in the $5\text{--}80^\circ$ ($2\theta_{\text{Cu}}$) range using a 0.02° ($2\theta_{\text{Cu}}$) step of a 1 s duration for routine characterization. For structural study (Rietveld refinement), data were collected in the $5\text{--}120^\circ$ ($2\theta_{\text{Cu}}$) range in steps of 0.02° ($2\theta_{\text{Cu}}$) with a constant counting time of 40 s.

Scanning electron micrographs were collected with a Hitachi S4500 field emission microscope with an accelerating voltage of 5.0 kV. In order to avoid charge accumulation during observation, a 2-nm-thick layer of platinum was deposited by cathodic sputtering on the surface of the materials.

The average oxidation state of the transition metal ions was determined by iodometric titration with $\text{Na}_2\text{S}_2\text{O}_8$. The average mass percentage of metal ions was checked by complexometric titration with ethylenediaminetetraacetic acid (EDTA).

X-ray photoelectron spectroscopy (XPS) spectra were recorded with a 220i-XL ESCALAB from VG. Powders were pressed onto indium foils and put under ultrahigh vacuum to reach the 10^{-8} Pa range. The monochromatized Al X-ray source (1486.6 eV) was used with a $250\text{-}\mu\text{m}$ spot size. The spectra were calibrated in relation to the internal graphite (C 1 s binding energy 284.1 eV). Fitting of the high-resolution spectra were provided through the Advantage program from Thermo Electron. Peaks were recorded with a constant pass energy $E_p=40$ eV.

Magnetic measurements were carried out with a Superconducting Quantum Interface Device (quantum design MPMS-5S). Magnetization vs field plots were recorded at 5 K over the $[-2000$ Oe; $+2000$ Oe] range. The H/M ratio (H applied field of 10,000 Oe and M measured magnetization) was measured in the $[5\text{--}300$ K] temperature range.

Electronic conductivity measurements were carried out on pellets (8 mm diam, pressed under 1000 Mpa but not sintered) with the four probe direct current method in the $70\text{--}300$ K temperature range.

For differential scanning calorimetry (DSC) experiments batteries were charged for each positive electrode material up to 4.1, 4.3, and 4.5 V, after a first cycle at C/20 rate between the higher cutoff voltage and 2 V. A small part of these electrodes (about 3 mg) still wetted by the electrolyte was introduced into a high-pressure crucible and sealed under argon atmosphere. The crucibles were then heat treated up to 400°C at a $10^\circ\text{C}/\text{min}$ heating rate.

Electrochemical properties of the $\text{Li}_{1+x}(\text{Ni}_{0.425}\text{Mn}_{0.425}\text{Co}_{0.15})_{1-x}\text{O}_2$ materials were examined in lithium cells containing lithium foil as negative electrode. The positive electrodes consisted of a mixture of 88 wt % active material, 10 wt % carbon black/graphite (1:1), and 2 wt % polytetrafluoroethylene as binder. Cells were assembled in an argon-filled dry box and cycled at room temperature in a galvanostatic mode at a constant C/20 rate (corresponding to a theoretical exchange of one electron per formula during charge or discharge).

Results and Discussion

Structural analysis

Figure 1 shows the XRD patterns of the $\text{Li}_{1+x}(\text{Ni}_{0.425}\text{Mn}_{0.425}\text{Co}_{0.15})_{1-x}\text{O}_2$ materials ($x_{\text{nom.}}=0, 0.03, 0.10, 0.20, 0.25, \text{ and } 0.33$). Some Miller indexes, the full width at half maximum (fwhm) of the (104) line, and the integral intensity ratio of the (003)/(104) diffraction lines are indicated. All the diffraction peaks except the small and broad ones between 19.5 and 26° ($2\theta_{\text{Cu}}$) were indexed based on a hexagonal cell ($\alpha\text{-NaFeO}_2$ type structure described in the space group $R\bar{3}m$). The narrowness of the

diffraction lines indicates a good crystallinity for these materials synthesized at high temperature and suggests a homogeneous distribution of all cations in the structure. Note that the (006)/(012) and (018)/(110) doublets get more and more separated upon increasing $x_{\text{nom.}}$ value. Moreover, the ratio $I_{(003)}/I_{(104)}$ increases with the $x_{\text{nom.}}$ value, which suggests that the more overlithiated the materials get, the more lamellar their structure becomes.

As shown on Fig. 1(b), small and broad diffraction lines were observed between 19.5 and 26° ($2\theta_{\text{Cu}}$). Note that they could have been at first attributed to Li_2MnO_3 , but the intense lines characteristic of Li_2MnO_3 were not present at $2\theta_{\text{Cu}}=37$ and 44.8° , showing that Li_2MnO_3 is not present in the materials as an impurity and that these small lines are probably due to the superlattice ordering of the Li, Ni, Mn, and Co ions in the transition metal layers, as suggested by Dahn and co-workers for the $\text{Li}[\text{Ni}_x\text{Li}_{(1/3-2x/3)}\text{Mn}_{(2/3-x/3)}]\text{O}_2$ materials.²⁶ Note that those small peaks grow slightly when the lithium content in the material increases, which may be explained by an increasing size of ordered domains or by a decreasing amount of defects in a perfectly ordered slab. This point is discussed in detail in Ref. 27.

Some Li_2O impurity was detected for the $x_{\text{nom.}}=0.25$ and 0.33 materials, which agrees with an $x_{\text{lim.th.}}=0.175$ theoretical limit for the overlithiation domain that corresponds to the cationic

distribution $\text{Li}_{1.175}\text{Ni}^{3+}_{0.35}\text{Mn}^{4+}_{0.35}\text{Co}^{3+}_{0.125}\text{O}_2$. Ni^{4+} and Co^{4+} ions are unlikely to exist in the pristine materials prepared at high temperature and under atmospheric pressure.²⁸ For the $x_{\text{nom.}}=0.20$ material, only some Li_2CO_3 traces were detected, in good agreement with an $x_{\text{nom.}}$ value closer to the theoretical solid solution limit.

Figure 2 shows the scanning electron micrographs (SEMs) obtained for the $\text{Li}_{1+x}(\text{Ni}_{0.425}\text{Mn}_{0.425}\text{Co}_{0.15})_{1-x}\text{O}_2$ ($x_{\text{nom.}}=0; 0.03; 0.10; 0.20$) materials. The average particle size increased strongly with the initial lithium excess used for the synthesis ($\sim 0.5 \mu\text{m}$ for the $x_{\text{nom.}}=0$ material and $\sim 1.5 \mu\text{m}$ for the $x_{\text{nom.}}=0.20$ material). The morphology evolved from quite individual particles for the $x_{\text{nom.}}=0$ material to more sintered particles for the $x_{\text{nom.}}=0.20$ material. On more enlarged views of the particles, some roughness could be observed on the surface of the $x_{\text{nom.}}=0.20$ material, which might be attributed to the Li_2CO_3 traces that were detected by XRD.

Elemental analyses (Li, Ni, Mn, and Co) of the $\text{Li}_{1+x}(\text{Ni}_{0.425}\text{Mn}_{0.425}\text{Co}_{0.15})_{1-x}\text{O}_2$ samples ($x_{\text{nom.}}=0, 0.03, 0.10, \text{ and } 0.20$) were carried out by inductively coupled plasma spectroscopy and the average transition metal oxidation state was measured by iodometric titration.²⁹ Using the average transition metal oxidation state and assuming that the chemical formula is $\text{Li}_{1+x}\text{M}_{1-x}\text{O}_2$ for these layered phases the real lithium concentration in these materials has been calculated. The results are reported in Table I. The chemical formula deduced from the average transition metal oxidation state values were found in rather good agreement with those obtained by chemical analyses. First of all, the results reported in Table I reveal that the average transition metal oxidation state increases with the initial lithium excess and thus show that extra lithium ions were incorporated within the structure and were substituted for transition metal ions. In LiMO_2 materials the average oxidation state of the transition metal ions is equal to 3; if $x \text{ M}^{3+}$ ions are replaced by $x \text{ Li}^+$ ions, then $2x \text{ M}^{3+}$ ions should be oxidized into $2x \text{ M}^{4+}$ ions in order to keep charge balance for the material. The formation of $\text{Li}_{1+x}\text{MO}_2$ -type phases was not considered as it would require the reduction of the average transition metal ion oxidation state with overlithiation; the opposite was observed. These results also reveal that the discrepancy between the nominal x values and those calculated from the average transition metal oxidation states increases with the initial lithium excess (Table I); it was attributed to lithium loss during heat-treatment. For instance, the real x value was found to be equal to 0.12 only for the $x_{\text{nom.}}=0.20$ material, whereas it was 0.08 for the $x_{\text{nom.}}=0.10$ material. Finally, the presence of small traces of lithium carbonate was detected for the $x_{\text{nom.}}=0.20$ material (Fig. 1(b)), despite a real x value lower than $x_{\text{lim.th.}}=0.175$, revealing that in our synthesis conditions (1000°C , 12 h, air) the experimental x limit of the solid solution domain is in fact ~ 0.12 . For $x \geq 0.12$ lithium carbonate or lithium oxide was observed as an impurity phase. Unpublished results obtained in our lab revealed that the synthesis of the $\text{Li}_{1+x}(\text{Ni}_{0.425}\text{Mn}_{0.425}\text{Co}_{0.15})_{1-x}\text{O}_2$ materials at increasing temperatures leads in fact to lower overlithiation due to higher lithium losses during the thermal treatment.

From this section, the real lithium concentrations are used in the $\text{Li}_{1+x}(\text{Ni}_{0.425}\text{Mn}_{0.425}\text{Co}_{0.15})_{1-x}\text{O}_2$ formula and are taken into account for the refinement of the XRD patterns by the Rietveld method. Note also that in a first step the nickel, manganese, and cobalt ions were assumed as expected from the solid-state chemistry point of view to be in these materials at the divalent/trivalent, tetravalent, and trivalent oxidation states, respectively.^{30,31,32,33,34}

In a previous report,²⁴ we refined the structure of $\text{LiNi}_{0.425}\text{Mn}_{0.425}\text{Co}_{0.15}\text{O}_2$ assuming a hexagonal cell ($\alpha\text{-NaFeO}_2$ type structure; S.G.: $R\bar{3}m$) and a cation mixing between the Li^+ and Ni^{2+} ions among the 3a and 3b sites so that the chemical formula can be written as $(\text{Li}_{1-z}\text{Ni}_z)_{3b}(\text{Li}_z\text{Ni}_{0.425-z}\text{Mn}_{0.425}\text{Co}_{0.15})_{3a}\text{O}_2$, in good agreement with an average transition metal oxidation state of 3.00. The z value was found to be equal to 0.08. Note that due to their similar ionic radii, the cationic mixing was assumed to occur between Li^+ and Ni^{2+} ions [$r(\text{Ni}^{2+})=0.69 \text{ \AA}$, $r(\text{Li}^+)=0.72 \text{ \AA}$]. As it will be reported elsewhere, this hypothesis was recently confirmed by neutron diffraction.²⁷

In good agreement with an increasing average oxidation state and thus the substitution of lithium ions for transition metal ions in the slabs, the general following formula was considered for the $\text{Li}_{1+x}(\text{Ni}_{0.425}\text{Mn}_{0.425}\text{Co}_{0.15})_{1-x}\text{O}_2$ materials: $(\text{Li}_{1-z}\text{Ni}_z)_{3b}(\text{Li}_{x+z}\text{Ni}_{0.425(1-x)-z}\text{Mn}_{0.425(1-x)}\text{Co}_{0.15(1-x)})_{3a}\text{O}_2$ where x (fixed value) is the overlithiation ratio determined by iodometric titration and z (refined value) the nickel occupancy in the lithium site. The presence of $z\text{Ni}^{2+}$ ions in the 3b site implies thus $z\text{Li}^+$ ions in the 3a site (i.e., an exchange between the $\text{Li}^+/\text{Ni}^{2+}$ ions). As a result, the total Li^+ concentration in the 3a site is equal to $x+z$. For the refinement of the XRD data, the 3a and 3b sites were constraint to be full. The total nickel concentration was constrained to $0.425(1-x)$; the manganese and cobalt concentrations were fixed to $0.425(1-x)$ and $0.15(1-x)$, respectively. The comparison between the experimental and the calculated XRD patterns is given in Fig. 3 for the $\text{LiNi}_{0.425}\text{Mn}_{0.425}\text{Co}_{0.15}\text{O}_2$ and the $\text{Li}_{1.12}(\text{Ni}_{0.425}\text{Mn}_{0.425}\text{Co}_{0.15})_{0.88}\text{O}_2$ phases. According to a good minimization of the differences, the structural model was shown to describe at least rather well the long-range structure for the $\text{Li}_{1+x}(\text{Ni}_{0.425}\text{Mn}_{0.425}\text{Co}_{0.15})_{1-x}\text{O}_2$ phases; however, the low-intensity peaks between 19.5 and 26° ($2\theta_{\text{Cu}}$), as shown in Fig. 4 for $\text{Li}_{1.12}(\text{Ni}_{0.425}\text{Mn}_{0.425}\text{Co}_{0.15})_{0.88}\text{O}_2$, were not taken into account by the structural model. Using electron diffraction, these small and diffuse peaks were shown to be due to the formation of orderings between the Li, Ni, Mn, and Co ions in the transition metal layers. These results are described and discussed more in detail in another one of our papers.²⁷

Table II gives the structural parameters determined for the $\text{Li}_{1+x}(\text{Ni}_{0.425}\text{Mn}_{0.425}\text{Co}_{0.15})_{1-x}\text{O}_2$ materials ($x=0, 0.03, 0.08$, and 0.12) by Rietveld refinement of their XRD data, whereas Table III summarizes the cationic distributions. A decrease in the amount of nickel ions in the interslab space was thus shown and confirmed the increasing lamellar character of the structure when overlithiation increased in $\text{Li}_{1+x}(\text{Ni}_{0.425}\text{Mn}_{0.425}\text{Co}_{0.15})_{1-x}\text{O}_2$. The increasing amount of Ni^{3+} ions in the slab for charge compensation reduces the possible exchange between lithium and nickel ions because the Ni^{3+} ions are rather more stable in the slab due to their difference in ionic radii with Li^+ ions [$r(\text{Ni}^{3+})=0.56 \text{ \AA}$, $r(\text{Li}^+)=0.72 \text{ \AA}$]. The variation of the amounts of Ni^{2+} ions in the slab and interslab space in $\text{Li}_{1+x}(\text{Ni}_{0.425}\text{Mn}_{0.425}\text{Co}_{0.15})_{1-x}\text{O}_2$ vs the overlithiation ratio x is reported in Fig. 5. These amounts decrease linearly and can be extrapolated to $x=0.186$ and 0.155 , respectively, and are close to the theoretical limit of the solid solution domain ($x_{\text{lim,th}}=0.175$). A continuous decrease of the lattice parameters is observed with an increasing overlithiation (x). The thicknesses of the LiO_2 interslab space $l_{(\text{LiO}_2)}$ and of the MO_2 slabs $S_{(\text{MO}_2)}$ were calculated from the cell parameter c_{hex} and the atomic coordinate for oxygen ions (z_{Ox}) (Table II). The decrease of a_{hex} and $S_{(\text{MO}_2)}$ results from the higher amount of Ni^{3+} ions in the slab to compensate for overlithiation and is in good agreement with a decrease of the average M–O distance (Table II). The increase of $l_{(\text{LiO}_2)}$ results from a decreasing amount of Ni^{2+} ions in the interslab space with overlithiation (x) and thus from a smaller screening between the oxygen layers of the interslab space. The variation of the c_{hex} parameter depends on the evolution of both $S_{(\text{MO}_2)}$ and $l_{(\text{LiO}_2)}$. As $S_{(\text{MO}_2)}$ decreases more strongly than $l_{(\text{LiO}_2)}$ increases, c_{hex} decreases. Note that such a large decrease of a_{hex} and c_{hex} parameters was also obtained for the $\text{Li}_{1+x}\text{Ni}_{1-x}\text{O}_2$ phases obtained under high oxygen partial pressure, it was associated with the oxidation of Ni^{3+} ions into Ni^{4+} ions stabilized by the presence of extra lithium ions in the materials.²⁸

Characterization of the transition metal ion oxidation states by XPS analyses

In order to confirm the oxidation states of the cations in these materials and the oxidation of Ni^{2+} ions into Ni^{3+} ions when the overlithiation increases, XPS experiments were performed on the $\text{Li}_{1+x}(\text{Ni}_{0.425}\text{Mn}_{0.425}\text{Co}_{0.15})_{1-x}\text{O}_2$ materials ($x=0$ and 0.12). Figure 6 shows the Co $2p_{3/2}$ and Mn $2p_{3/2}$ XPS spectra for these materials. The binding energies were obtained by fitting the experimental curves. The calculated curve profile was defined as a combination of Gaussian and Lorentzian distributions with an anisotropic contribution that takes into account the asymmetrical shape usually observed for the transition metal 2p lines.³⁵ An experimental binding energy value of $\sim 780 \text{ eV}$ was obtained for the Co $2p_{3/2}$ spectra of $\text{LiNi}_{0.425}\text{Mn}_{0.425}\text{Co}_{0.15}\text{O}_2$ and $\text{Li}_{1.12}(\text{Ni}_{0.425}\text{Mn}_{0.425}\text{Co}_{0.15})_{0.88}\text{O}_2$. Note that this value was very close to that obtained for LiCoO_2 (779.6 eV).³⁶ Because the binding energies corresponding to trivalent and tetravalent cobalt ions cannot be discriminated, the fwhm of the Co $2p_{3/2}$ was measured (2.2 eV for both materials) and was found close to that measured for LiCoO_2 (2.4 eV) where all the cobalt ions are in the trivalent state, in contrast with the metallic

$\text{Li}_{0.6}\text{CoO}_2$ (3.7 eV) where the cobalt ions are present at a higher oxidation state (average oxidation state 3.4). Therefore the cobalt ions in the $\text{Li}_{1+x}(\text{Ni}_{0.425}\text{Mn}_{0.425}\text{Co}_{0.15})_{1-x}\text{O}_2$ materials ($x=0$ and $x=0.12$) are trivalent.³⁶ Note that from a chemical point of view, Co^{4+} ions were not expected to be present in these materials that were synthesized at high temperature. Concerning the Mn $2p_{3/2}$ spectrum, an experimental binding energy of ~ 642.5 eV and a fwhm value of 2.8 eV were found for both $\text{LiNi}_{0.425}\text{Mn}_{0.425}\text{Co}_{0.15}\text{O}_2$ and $\text{Li}_{1.12}(\text{Ni}_{0.425}\text{Mn}_{0.425}\text{Co}_{0.15})_{0.88}\text{O}_2$. These values were consistent with the presence of Mn^{4+} ions in these materials and with results recently obtained by some of us for different manganese-rich materials.³⁷ Note that the intensity and thus the resolution obtained for the Co $2p_{3/2}$ and Mn $2p_{3/2}$ XPS spectra were much lower than that of the Ni $2p_{3/2}$ due to lower sensibility factors for Mn and Co and hence to a smaller accuracy for the binding energy determination. Figure 7 shows the Ni $2p_{3/2}$ XPS spectra for these materials. For the $x=0$ material, the Ni binding energy (854.2 eV) is close to the value reported in the literature for NiO. For the $x=0.12$ material, the Ni $2p_{3/2}$ peak fitting procedure reveals two contributions, one at 854.2 eV corresponding to the NiO binding energy and another at 855.2 eV consistent with the presence of Ni^{3+} ions.³⁸ The $\text{Ni}^{3+}/(\text{Ni}^{2+} + \text{Ni}^{3+})$ ratio estimated from this spectrum for the $x=0.12$ material was ~ 0.58 , which was in agreement with the theoretical ratio of 0.64 calculated from the cationic distribution reported in Table III. Note that some $\text{Ni}^{3+}/(\text{Ni}^{2+} + \text{Ni}^{3+})$ ratio values were found lower than 0.58 depending on the analysis area, which suggests that the surface composition of $\text{Li}_{1.12}(\text{Ni}_{0.425}\text{Mn}_{0.425}\text{Co}_{0.15})_{0.88}\text{O}_2$ might be different from the bulk one. XPS analyses confirmed thus that cobalt and manganese ions are present at the trivalent and tetravalent oxidation states, respectively, in these $\text{Li}_{1+x}(\text{Ni}_{0.425}\text{Mn}_{0.425}\text{Co}_{0.15})_{1-x}\text{O}_2$ materials and that overlithiation leads to an oxidation of Ni^{2+} ions into Ni^{3+} ions.

Magnetic properties

Figure 8 shows the comparison of the hysteresis loops vs magnetic field for $\text{Li}_{1+x}(\text{Ni}_{0.425}\text{Mn}_{0.425}\text{Co}_{0.15})_{1-x}\text{O}_2$ ($x=0, 0.03, 0.08, \text{ and } 0.12$). In a previous paper²⁴ the magnetic properties of the $x=0$ material were shown to be similar to those of $\text{LiNi}_{1/2}\text{Mn}_{1/2}\text{O}_2$.³⁹ The results reported in Fig. 8 show that when overlithiation increases in the $\text{Li}_{1+x}(\text{Ni}_{0.425}\text{Mn}_{0.425}\text{Co}_{0.15})_{1-x}\text{O}_2$ system, the hysteresis slit width decreases. This evolution is in good agreement with the decrease in the amount of Ni^{2+} ions in the interslab space ($z=0.02$ for $x=0.12$ vs $z=0.08$ for $x=0$) and with the increasing concentration of Ni^{3+} ions (64% of total nickel amount for $x=0.12$ vs 0% for $x=0$) (Table III). Previous studies have shown that the presence of paramagnetic ions in the interslab space leads to strong 180° antiferromagnetic M–O–M interactions between the slab and the interslab space and thus to the formation of ferrimagnetic clusters.^{8,39,40}

Moreover, as shown in Fig. 9, the evolution of the H/M ratio (H the applied field and M the measured magnetization) vs temperature is characteristic of a Curie-Weiss behavior above 175 K. For the $x=0.00$ and 0.03 compositions, the shape of the curve is characteristic of a ferrimagnetic character; for example, $T_c=82$ K and $\theta_p=-110$ K for the $[\text{Li}_{0.92}\text{Ni}_{0.08}]_{3b}[\text{Li}_{0.08}\text{Ni}_{0.345}\text{Mn}_{0.425}\text{Co}_{0.15}]_{3a}\text{O}_2$ material. For the $x=0.08$ and 0.12 compositions, when the amount of lithium ions in the slab increases, the materials are paramagnetic in the whole (5–300 K) temperature range, despite the presence of 0.03 and 0.02 extra Ni^{2+} ions in the interslab space, respectively. The presence of a large amount of diamagnetic ions in the slab for these materials [$(x+z)\text{Li}^+$ and $0.15(1-x)\text{Co}^{3+}$] tends to decrease the formation of ferrimagnetic clusters around the extra Ni^{2+} ions in the interslab space and thus explains that antiferromagnetic interactions are predominant, in agreement with the negative value observed for θ_p .

The theoretical Curie constants were calculated using the cationic distributions determined by refinement by the Rietveld method of the XRD data and are compared to the experimental ones in Table IV. Good agreements between theoretical and experimental values were obtained.

Therefore the magnetic measurements confirmed the chemical formula and the cationic distributions (i.e., the presence of extra Ni^{2+} ions in the interslab space) determined from the XRD data.

Electronic conductivity

Figure 10 shows the variation of the electronic conductivity vs reciprocal temperature for the $\text{Li}_{1+x}(\text{Ni}_{0.425}\text{Mn}_{0.425}\text{Co}_{0.15})_{1-x}\text{O}_2$ materials. In all cases, a semiconducting behavior is observed because the conductivity remains thermally activated. Nevertheless, increasing lithium content in the structure leads to a strong increase in the electronic conductivity. Because the conductivity measurements were carried out on unsintered pellets, as shown by the SEM micrographs in Fig. 2, the particles get more sintered with increasing overlithiation; it leads to a better electronic contact

between them and hence to a smaller resistive contribution of the grain boundaries. Nevertheless, such a huge conductivity variation ($\sigma \sim 10^{-9}$ S/cm to $\sigma = 10^{-4}$ S/cm at room temperature) can not only be attributed to the decrease in the grain boundary number. As shown by Carlier *et al.*,⁴¹ sintering a pellet of $O_3\text{-Li}_{0.60}\text{CoO}_2$ resulted only in a conductivity increase from $\sigma \sim 10^{-1}$ to $\sigma \sim 10^{0.5}$ S/cm. Increasing substitution of lithium ions for the transition metal ions in these $\text{Li}_{1+x}(\text{Ni}_{0.425}\text{Mn}_{0.425}\text{Co}_{0.15})_{1-x}\text{O}_2$ materials leads, for charge compensation, to oxidation of Ni^{2+} ions ($d^8 t_{2g}^6 e_g^2$) into Ni^{3+} ions ($d^7 t_{2g}^6 e_g^1$) and also to a decrease in the Ni–O bond length. This suggests an electronic hopping between Ni^{2+} and Ni^{3+} ions, which is believed to explain mainly this electronic conductivity increase. For the $x=0.00$ composition that contains Ni^{2+} , Co^{3+} , and Mn^{4+} ions, the conductivity is low; the hopping is unlikely to occur because the electronic transfer between different types of ions is difficult. Upon overlithiation the $\text{Ni}^{2+}/\text{Ni}^{3+}$ ratio increases and thus allows the electronic hopping to occur. Nevertheless, the activation energy (0.2 eV) remains quite high. This behavior results from the presence of Li^+ , Co^{3+} , and Mn^{4+} ions that are assumed to be randomly distributed in the slab and that are uneffective for the conductivity process.

Electrochemical behavior

Figure 11 compares the variation of the cell voltage vs lithium composition for $\text{Li}_{1+x}(\text{Ni}_{0.425}\text{Mn}_{0.425}\text{Co}_{0.15})_{1-x}\text{O}_2$ materials ($x=0$ and 0.12) in galvanostatic mode at the constant C/20 rate in the 2–4.3 V potential range. Initial discharge capacities of 158 and 120 mAh/g were obtained, respectively. The large decrease in the reversible capacity can be explained by the increase of the transition metal average oxidation state in the starting materials with overlithiation (oxid. state=3.25 for $x=0.12$ vs oxid. state=3.00 for $x=0$), thus leading to a decrease of the total exchangeable electron number. Rather small irreversible capacity and weak polarization (~ 0.12 V) are observed for both materials, despite the presence of 0.08 of nickel ions in the interslab space for the $x=0$ material. For the lithium nickelate $\text{Li}_{1-z}\text{Ni}_{1+z}\text{O}_2$, the presence of z extra nickel ions in the lithium sites was shown to strongly hinder lithium diffusion due to local contractions of the interslab space after the first charge, thus leading to increasing irreversible capacity and rapid loss of cyclability with increasing z .⁴² In these $\text{Li}_{1+x}(\text{Ni}_{0.425}\text{Mn}_{0.425}\text{Co}_{0.15})_{1-x}\text{O}_2$ materials, nickel ions are present in the lithium sites but there are also lithium ions in the transition metal sites; therefore, a 3D lithium diffusion can occur through the host structure with a diffusion mechanism different from that previously observed for $\text{Li}_{1-z}\text{Ni}_{1+z}\text{O}_2$ and especially not so sensitive to the presence of nickel ions in the interslab space. The derivative curve $-dx/|dV|=f(V)$ does not exhibit any sharp peak, thus showing that no first-order phase transition occurs upon cycling in the 2–4.3 V potential range for these materials. The characterization of the structural and redox changes for a $\text{Li}_{1.12}(\text{Ni}_{0.425}\text{Mn}_{0.425}\text{Co}_{0.15})_{0.88}\text{O}_2$ material during the first cycle in the 2–5 V potential range is now in progress in our lab. These results will be discussed in detail in a forthcoming paper.

Thermal stability

Figure 12 shows the DSC profiles for the $\text{Li}_y\text{Ni}_{0.425}\text{Mn}_{0.425}\text{Co}_{0.15}\text{O}_2$ ($y=0.5, 0.4,$ and 0.34) and $\text{Li}_y(\text{Ni}_{0.425}\text{Mn}_{0.425}\text{Co}_{0.15})_{0.88}\text{O}_2$ ($y=0.73, 0.66,$ and 0.42) materials, recovered from the lithium cells charged to 4.1, 4.3, and 4.5 V, respectively. Before considering these results, one has to note that the deintercalated materials were still wetted by the ternary electrolyte [LiPF_6 1 M in a mixture of (PC:EC:DMC) (1:1:3)] during the thermal analyses. The DSC profiles are thus more an indirect observation of the thermal stability of the deintercalated materials, they show the exothermic peaks associated with the reaction of oxygen with the electrolyte components, that oxygen being lost by the material during its degradation upon increasing temperature. Because the reactions associated with the electrolyte are highly exothermic in comparison with those associated with the material itself, the peaks observed on the DSC profiles are not representative of the thermal degradation mechanism for the material. They just indicate the temperature up to which a material is stable, and the energy evolved from the reaction between the material and the electrolyte available. When the reaction associated with the material degradation is highly exothermic, reactions of oxygen with the different electrolyte components can be initiated all together and only a large and unique peak can be observed. If the reaction involving the material is less exothermic, then the reactions with the electrolyte can be separated and various peaks can be observed on the DSC profiles.

The exothermic reaction associated with the electrolyte and initiated by the decomposition of the deintercalated $\text{Li}_y\text{Ni}_{0.425}\text{Mn}_{0.425}\text{Co}_{0.15}\text{O}_2$ materials starts at $\sim 320^\circ\text{C}$ (onset temperature) whatever the cutoff voltage in charge. However, the energy evolved from the exothermic reaction increases with the cutoff voltage. In the case of the deintercalated $\text{Li}_y(\text{Ni}_{0.425}\text{Mn}_{0.425}\text{Co}_{0.15})_{0.88}\text{O}_2$ materials, the reaction involving the electrolyte starts at a lower onset temperature (from ~ 270 to $\sim 260^\circ\text{C}$ when

the cutoff voltage increases) and is much more exothermic with an increasing evolved energy upon increasing cutoff voltage, as shown in Fig. 12. Nevertheless, their thermal stability is much higher than that of Li_xCoO_2 .²⁰ Table V gives the evolution of the lithium content and the $(\text{Ni}^{4+} + \text{Co}^{4+})/M$ ratio (M for transition metal ions) as a function of the cutoff voltage. The Ni^{4+} and Co^{4+} ions are highly unstable at high temperature whereas the other ions (Ni^{2+} , Ni^{3+} , Co^{3+} , and Mn^{4+}) are more stable. As the amount of Ni^{4+} and Co^{4+} ions increases, the onset temperature of the exothermic reaction decreases. The difference in the thermal effects recorded on the DSC profiles between the $\text{Li}_y\text{Ni}_{0.425}\text{Mn}_{0.425}\text{Co}_{0.15}\text{O}_2$ and $\text{Li}_y(\text{Ni}_{0.425}\text{Mn}_{0.425}\text{Co}_{0.15})_{0.88}\text{O}_2$ materials can be explained through the amount of unstable cations present in the materials. Increasing overlithiation for $\text{Li}_{1+x}(\text{Ni}_{0.425}\text{Mn}_{0.425}\text{Co}_{0.15})_{1-x}\text{O}_2$ leads to an initial higher average oxidation state and thus to a larger amount of unstable cations (Ni^{4+} and Co^{4+}) after the lithium ion deintercalation and a smaller thermal stability in the highly deintercalated states. Therefore, the exothermic reaction induced by the material degradation tends to initiate the reaction with the electrolyte components at a lower onset temperature. $\text{Li}_y\text{Ni}_{0.425}\text{Mn}_{0.425}\text{Co}_{0.15}\text{O}_2$ materials have a quite small amount of lithium ions in the structure but less than 23% of unstable cations. On the contrary, the $\text{Li}_y(\text{Ni}_{0.425}\text{Mn}_{0.425}\text{Co}_{0.15})_{0.88}\text{O}_2$ materials have still a large amount of lithium ions in their structure but more than 29% of the transition metal ions at unstable oxidation states. Increasing overlithiation for $\text{Li}_{1+x}(\text{Ni}_{0.425}\text{Mn}_{0.425}\text{Co}_{0.15})_{1-x}\text{O}_2$ leads to an initial higher average oxidation state and thus a larger amount of unstable cations (Ni^{4+} and Co^{4+}) at high potential and a smaller thermal stability in the highly deintercalated states, despite a larger amount of lithium in the material. At 4.5 V/Li, for about the same amount of lithium deintercalated from the structure (0.66 deintercalated lithium ions for $\text{Li}_y\text{Ni}_{0.425}\text{Mn}_{0.425}\text{Co}_{0.15}\text{O}_2$ and 0.70 for $\text{Li}_y(\text{Ni}_{0.425}\text{Mn}_{0.425}\text{Co}_{0.15})_{0.88}\text{O}_2$, there was ~23% of unstable cations for $\text{Li}_y\text{Ni}_{0.425}\text{Mn}_{0.425}\text{Co}_{0.15}\text{O}_2$ vs ~55% of unstable cations for $\text{Li}_y(\text{Ni}_{0.425}\text{Mn}_{0.425}\text{Co}_{0.15})_{0.88}\text{O}_2$, which explains the difference of ~60°C in thermal stability. A recent study of different substituted lithium nickelate systems performed by some of us has shown that the thermal stability at the charged states strongly depends on the nature of the cations present in the slabs and especially on their relative stability at different oxidation states.^{6,9}

Conclusions

Well-crystallized $\text{Li}_{1+x}(\text{Ni}_{0.425}\text{Mn}_{0.425}\text{Co}_{0.15})_{1-x}\text{O}_2$ ($x=0, 0.03, 0.08, \text{ and } 0.12$) materials have successfully been synthesized by a coprecipitation method. The refinement of their crystal structure in the $R\bar{3}m$ space group showed a decrease in the Ni occupancy in the Li layers with increasing overlithiation (x). Some small and broad diffraction lines clearly observed in the 19.5–26° ($2\theta_{\text{Cu}}$) range for the most overlithiated materials were not taken into account by this structural model. They suggest the presence of a superlattice ordering that was studied in detail in Ref. 27. Redox titrations and XPS spectra showed the oxidation of Ni^{2+} ions into Ni^{3+} ions with increasing overlithiation (x) for these $\text{Li}_{1+x}(\text{Ni}_{0.425}\text{Mn}_{0.425}\text{Co}_{0.15})_{1-x}\text{O}_2$ materials, the manganese and cobalt ions being at the tetravalent and trivalent states, respectively. Magnetic measurements confirmed the chemical formula and the cationic distributions determined from the XRD data for the $\text{Li}_{1+x}(\text{Ni}_{0.425}\text{Mn}_{0.425}\text{Co}_{0.15})_{1-x}\text{O}_2$ materials. The electronic conductivity increase with overlithiation for these materials was attributed to a hopping between Ni^{2+} and Ni^{3+} ions and to a lesser extent to more sintered particles with overlithiation. The electrochemical properties of these materials were shown to be strongly dependant on the lithium content in the material. The smallest reversible capacity was observed for the most lithiated material, which was explained by the limited number of exchangeable electrons due to the higher initial average metal oxidation state. The $\text{Li}_{1+x}(\text{Ni}_{0.425}\text{Mn}_{0.425}\text{Co}_{0.15})_{1-x}\text{O}_2$ materials were shown to be thermally more stable than LiCoO_2 . However, their thermal stability decreased with overlithiation due to a higher initial average transition metal ion oxidation state and hence to a higher amount of unstable cations for the $\text{Li}_y(\text{Ni}_{0.425}\text{Mn}_{0.425}\text{Co}_{0.15})_{1-x}\text{O}_2$ deintercalated phases.

Acknowledgments

The authors are grateful to Michel Ménétrier (ICMCB) and A. Lecerf (INSA, Rennes, France) for fruitful discussions, to C. Denage (ICMCB) for scanning electron microscopy and technical assistance, to Ph. Dagault (ICMCB) for thermal analyses, to R. Decourt (ICMCB) for electrical measurements, to SAFT and Région Aquitaine for financial support.

CNRS assisted in meeting the publication costs of this article.

References

1. J. P. Pérès, C. Delmas, A. Rougier, M. Broussely, F. Pertont, P. Biensan, and P. Willmann, *J. Phys. Chem. Solids*, **57**, 1057 _1996_.
2. M. Broussely, F. Pertont, P. Biensan, J. M. Bodet, J. Labat, A. Lecerf, C. Delmas, A. Rougier, and J. P. Pérès, *J. Power Sources*, **54**, 109 _1995_.
3. J. R. Dahn, E. W. Fuller, M. Obrovac, and U. Von Sacken, *Solid State Ionics*, **69**, 265 _1994_.
4. T. Ohzuku, A. Ueda, and M. Kouguchi, *J. Electrochem. Soc.*, **142**, 4033 _1995_.
5. H. Arai, S. Okada, Y. Sakurai, and J. Yamaki, *Solid State Ionics*, **109**, 295 _1998_.
6. M. Guilmard, L. Croguennec, D. Denux, and C. Delmas, *Chem. Mater.*, **15**, 4476 _2003_.
7. M. Broussely, P. Blanchard, P. Biensan, J. P. Planchat, K. Nechev, and R. J. Staniewicz, *J. Power Sources*, **119**, 859 _2003_.
8. M. Guilmard, C. Pouillierie, L. Croguennec, and C. Delmas, *Solid State Ionics*, **160**, 39 _2003_.
9. M. Guilmard, L. Croguennec, and C. Delmas, *Chem. Mater.*, **15**, 4484 _2003_.
10. Z. H. Lu, D. D. MacNeil, and J. R. Dahn, *Electrochem. Solid-State Lett.*, **4**, A191 _2001_.
11. Z. H. Lu and J. R. Dahn, *J. Electrochem. Soc.*, **149**, A1454 _2002_.
12. Y. Grincourt, C. Storey, and I. J. Davidson, *J. Power Sources*, **97-98**, 711 _2001_.
13. C. Storey, I. Kargina, Y. Grincourt, I. J. Davidson, Y. C. Yoo, and D. Y. Seung, *J. Power Sources*, **97-98**, 541 _2001_.
14. Z. H. Lu and J. R. Dahn, *J. Electrochem. Soc.*, **149**, 815 _2002_.
15. Y. K. Sun, M. G. Kim, S. H. Kang, and K. Amine, *J. Mater. Chem.*, **13**, 319 _2003_.
16. P. G. Bruce, A. R. Armstrong, and R. L. Gitzendanner, *J. Mater. Chem.*, **9**, 193 _1999_.
17. F. Capitaine, P. Gravereau, and C. Delmas, *Solid State Ionics*, **89**, 197 _1996_.
18. L. Croguennec, P. Deniard, and R. Brec, *J. Electrochem. Soc.*, **144**, 3323 _1997_.
19. C. Delmas and F. Capitaine, in Extended Abstracts of the 8th International Meeting on Lithium Batteries, Nagoya, Japan _1996_.
20. C. W. Lee, Y. K. Sun, and J. Prakash, *Electrochim. Acta*, **49**, 4425 _2004_.
21. T. Ohzuku and Y. Makimura, *Chem. Lett.*, **2001**, 642.
22. B. J. Hwang, Y. W. Tsai, D. Carlier, and G. Ceder, *Chem. Mater.*, **15**, 3676 _2003_.
23. Z. X. Wang, Y. C. Sun, L. Q. Chen, and X. J. Huang, *J. Electrochem. Soc.*, **151**, A914 _2004_.
24. N. Tran, L. Croguennec, C. Jordy, P. Biensan, and C. Delmas, *Solid State Ionics*, **176**, 1539 _2005_.
25. D. Caurant, N. Baffier, B. Garcia, and J. P. Pereira-Ramos, *Solid State Ionics*, **91**,

45 _1996_.

26. Z. H. Lu, L. Y. Beaulieu, R. A. Donaberger, C. L. Thomas, and J. R. Dahn, *J. Electrochem. Soc.*, **149**, A778 _2002_.

27. N. Tran, L. Croguennec, F. Weill, and C. Delmas, *J. Mater. Chem.*, To be submitted.

28. R. Stoyanova, E. Zhecheva, R. Alcantara, J. L. Tirado, G. Bromiley, F. Bromiley, and T. B. Ballaran, *Solid State Ionics*, **161**, 197 _2003_.

29. S. Venkatraman and A. Manthiram, *Chem. Mater.*, **15**, 5003 _2003_.

30. F. Tournadre, L. Croguennec, I. Saadoune, F. Weill, Y. Shao-Horn, P. Willmann, and C. Delmas, *Chem. Mater.*, **16**, 1411 _2004_.

31. J. K. Ngala, N. A. Chernova, M. M. Ma, M. Mamak, P. Y. Zavalij, and M. S. Whittingham, *J. Mater. Chem.*, **14**, 214 _2004_.

32. W. S. Yoon, C. P. Grey, M. Balasubramanian, X. Q. Yang, D. A. Fischer, and J. McBreen, *Electrochem. Solid-State Lett.*, **7**, A53 _2004_.

33. K. M. Shaju, G. V. S. Rao, and B. V. R. Chowdari, *Electrochim. Acta*, **48**, 1505 _2003_.

34. W. Yoon, Y. Paik, X. Yang, M. Balasubramanian, J. McBreen, and C. Grey, *Electrochem. Solid-State Lett.*, **5**, A263 _2002_.

35. *Practical Surface Analyses*, 2nd ed., Vol. 1, *Auger and X-Ray Photoelectron Spectroscopy*, D. Briggs and M. P. Seah, Editors, Wiley, New York _1990_.

36. J. C. Dupin, D. Gonbeau, I. Martin-Litas, P. Vinatier, and A. Levasseur, *J. Electron Spectrosc. Relat. Phenom.* **120**, 55 _2001_.

37. Unpublished results obtained in collaboration with D. Gonbeau and company, Pau University, France.

38. K. S. Kim and R. E. Davis, *J. Electron Spectrosc. Relat. Phenom.*, **1**, 251 _1973_.

39. H. Kobayashi, H. Sakaebe, H. Kageyama, K. Tatsumi, Y. Arachi, and T. Kamiyama, *J. Mater. Chem.*, **13**, 590 _2003_.

40. A. L. Barra, G. Chouteau, A. Stepanov, A. Rougier, and C. Delmas, *Eur. Phys. J. B*, **7**, 551 _1999_.

41. D. Carlier, I. Saadoune, M. Menetrier, and C. Delmas, *J. Electrochem. Soc.*, **149**, A1310 _2002_.

42. A. Rougier, P. Gravereau, and C. Delmas, *J. Electrochem. Soc.*, **143**, 1168 _1996_.

43. J. F. Berar and P. Lelann, *J. Appl. Crystallogr.*, **24**, 1 _1991_.

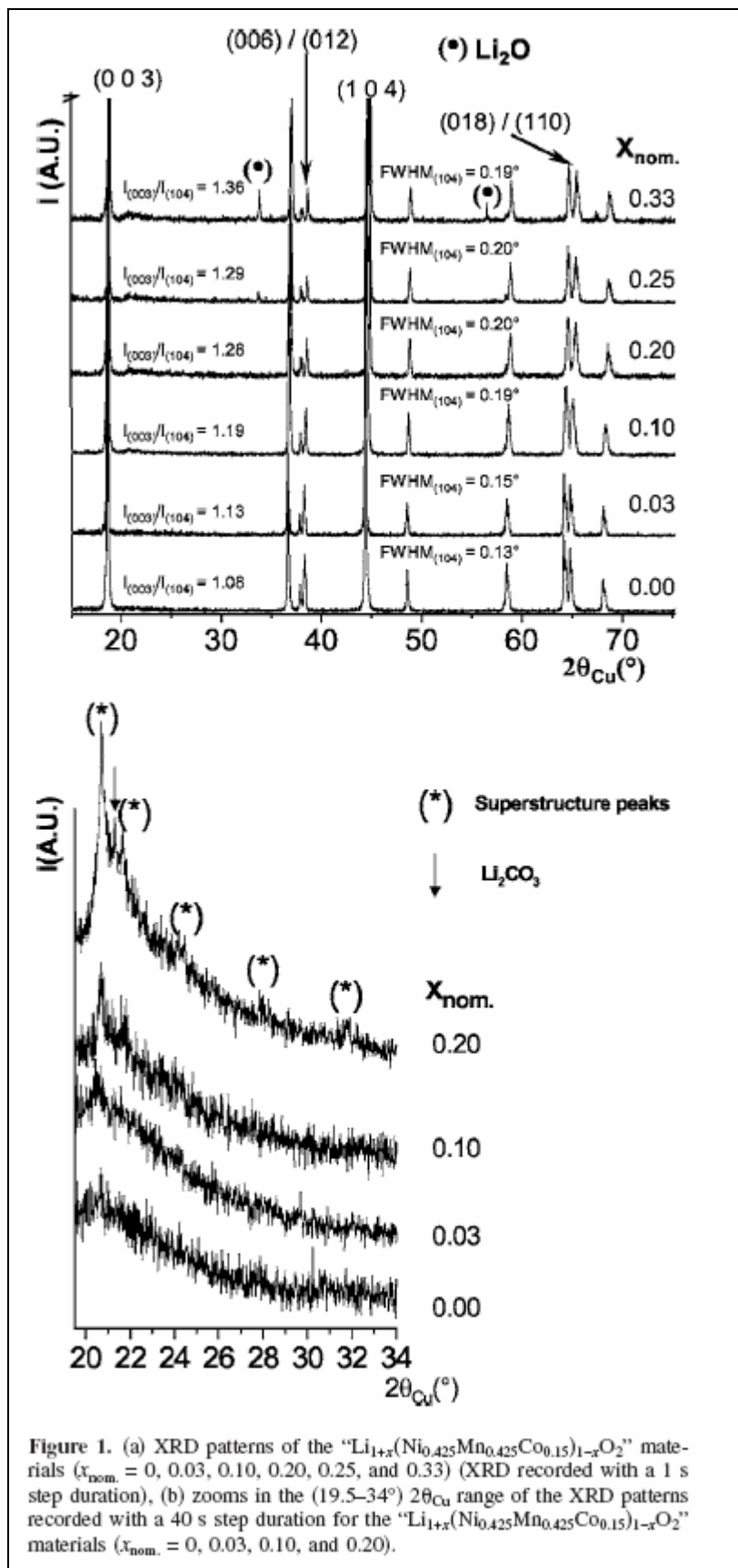


Figure 1. (a) XRD patterns of the " $\text{Li}_{1+x}(\text{Ni}_{0.425}\text{Mn}_{0.425}\text{Co}_{0.15})_{1-x}\text{O}_2$ " materials ($x_{\text{nom.}} = 0, 0.03, 0.10, 0.20, 0.25,$ and 0.33) (XRD recorded with a 1 s step duration), (b) zooms in the ($19.5\text{--}34^\circ$) $2\theta_{\text{Cu}}$ range of the XRD patterns recorded with a 40 s step duration for the " $\text{Li}_{1+x}(\text{Ni}_{0.425}\text{Mn}_{0.425}\text{Co}_{0.15})_{1-x}\text{O}_2$ " materials ($x_{\text{nom.}} = 0, 0.03, 0.10,$ and 0.20).

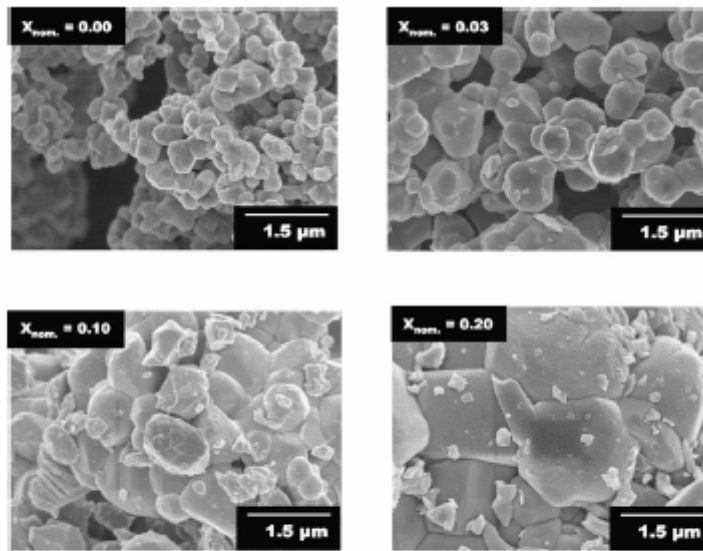


Figure 2. SEMs obtained for the $\text{Li}_{1+x}(\text{Ni}_{0.425}\text{Mn}_{0.425}\text{Co}_{0.15})_{1-x}\text{O}_2$ materials ($x_{\text{nom.}} = 0, 0.03, 0.10, 0.20$).

Table I. Average oxidation state ($\text{oxid. state}_{(\text{titrated})}$) obtained by iodometric titration and real overlithiation ratio ($x_{(\text{real})}$) determined for the " $\text{Li}_{1+x}(\text{Ni}_{0.425}\text{Mn}_{0.425}\text{Co}_{0.15})_{1-x}\text{O}_2$ " materials ($x_{\text{nom.}} = 0, 0.03, 0.10, \text{ and } 0.20$).

$x_{\text{nom.}}$	Oxid. state _(target)	Oxid. state _(titrated)	$x_{(\text{real})}$ ^a
0.00	3.00	3.00	0.00
0.03	3.07	3.08	0.03
0.10	3.22	3.15	0.08
0.20	3.50	3.25	0.12

^a The real extra lithium content ($x_{(\text{real})}$) was calculated assuming the formula $\text{Li}_{1+x}\text{M}_{1-x}\text{O}_2$.

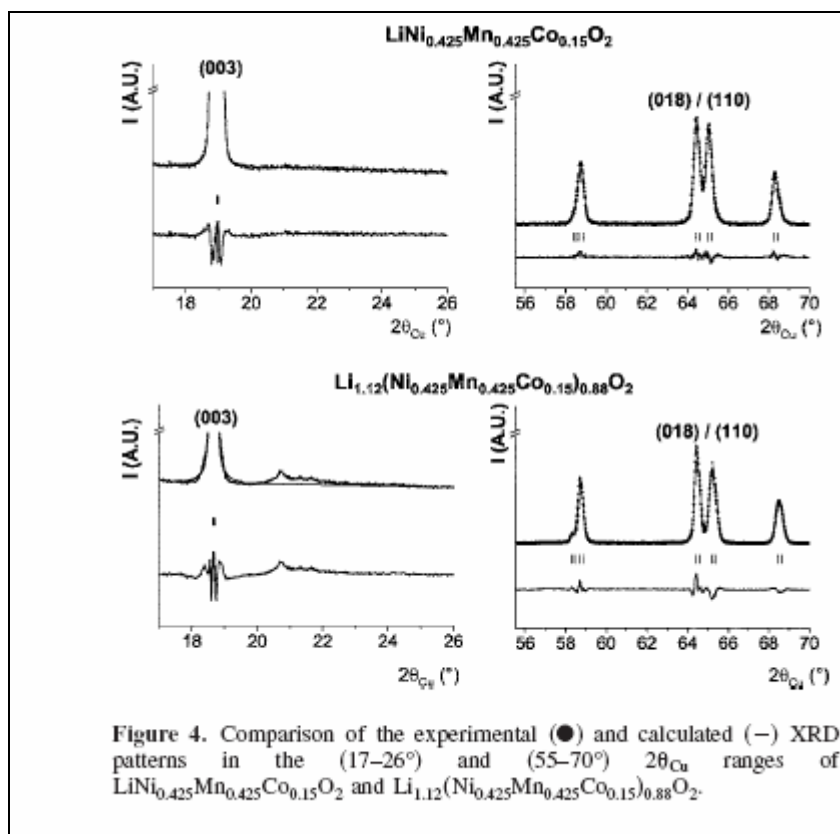
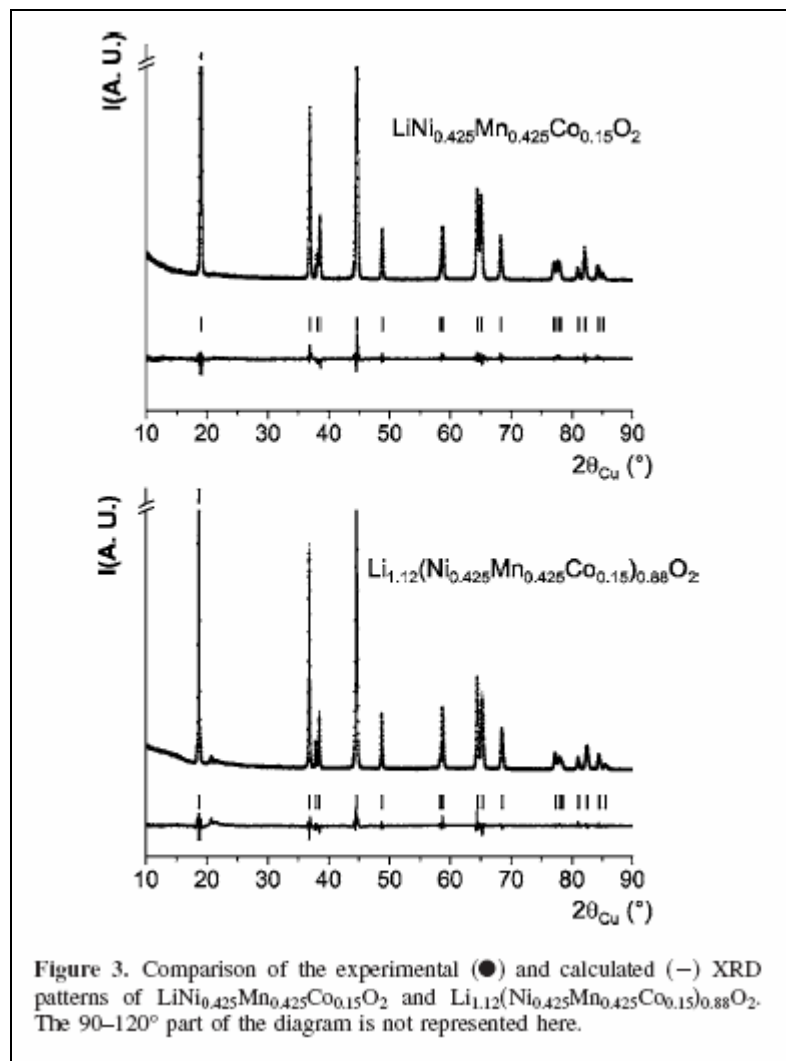


Table II. Structural parameters determined for the $\text{Li}_{1+x}(\text{Ni}_{0.425}\text{Mn}_{0.425}\text{Co}_{0.15})_{1-x}\text{O}_2$ materials ($x = 0, 0.03, 0.08, \text{ and } 0.12$) by the Rietveld refinement of their X-ray data.^a

X	$a_{\text{hex.}}$ (Å)	$c_{\text{hex.}}$ (Å)	$z_{\text{ox.}}$	$S_{(\text{MO}_2)}$ (Å) ^b	$I_{(\text{LiO}_2)}$ (Å) ^c	M-O (Å)
0.00	2.8797(1)	14.287(1)	0.2574(2)	2.17(2)	2.60(2)	1.99(1)
0.03	2.8739(1)	14.261(1)	0.2581(4)	2.15(2)	2.61(2)	1.98(1)
0.08	2.8687(1)	14.254(1)	0.2582(2)	2.14(2)	2.61(2)	1.97(1)
0.12	2.8580(1)	14.222(1)	0.2586(4)	2.13(2)	2.62(2)	1.96(1)

^a The standard deviation was multiplied by the Scorr parameter to correct for local correlations.⁴³

^b Slab thickness: $S_{(\text{MO}_2)} = 2(1/3 - z_{\text{ox.}})c_{\text{hex.}}$; $z_{\text{ox.}}$, the atomic coordinate of oxygen ions.

^c Interslab space thickness: $I_{(\text{LiO}_2)} = c_{\text{hex.}}/3 - S_{(\text{MO}_2)}$

Table III. Cationic distributions determined for the $\text{Li}_{1+x}(\text{Ni}_{0.425}\text{Mn}_{0.425}\text{Co}_{0.15})_{1-x}\text{O}_2$ materials ($x = 0, 0.03, 0.08, \text{ and } 0.12$) by the Rietveld refinement of their X-ray data. The $\text{Ni}^{2+}/\text{Ni}^{3+}$ balance is obtained from the charge compensation.

X	Interslab		Slab				
	Li^+	Ni^{2+}	Li^+	Ni^{2+}	Ni^{3+}	Mn^{4+}	Co^{3+}
0.00	0.922	0.078	0.078	0.347	0.000	0.425	0.150
0.03	0.940	0.060	0.090	0.284	0.068	0.413	0.145
0.08	0.967	0.033	0.113	0.198	0.160	0.391	0.138
0.12	0.980	0.020	0.140	0.114	0.240	0.374	0.132

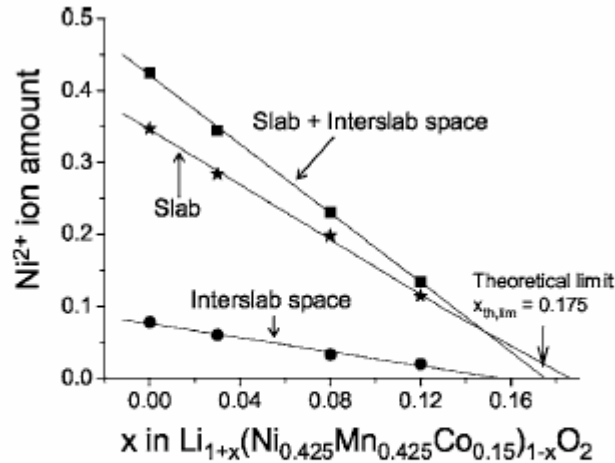


Figure 5. Evolution vs the overlithiation ratio (x) of the amounts of Ni^{2+} ions present in the slab, in the interslab space, and globally in the $\text{Li}_{1+x}(\text{Ni}_{0.425}\text{Mn}_{0.425}\text{Co}_{0.15})_{1-x}\text{O}_2$ materials.

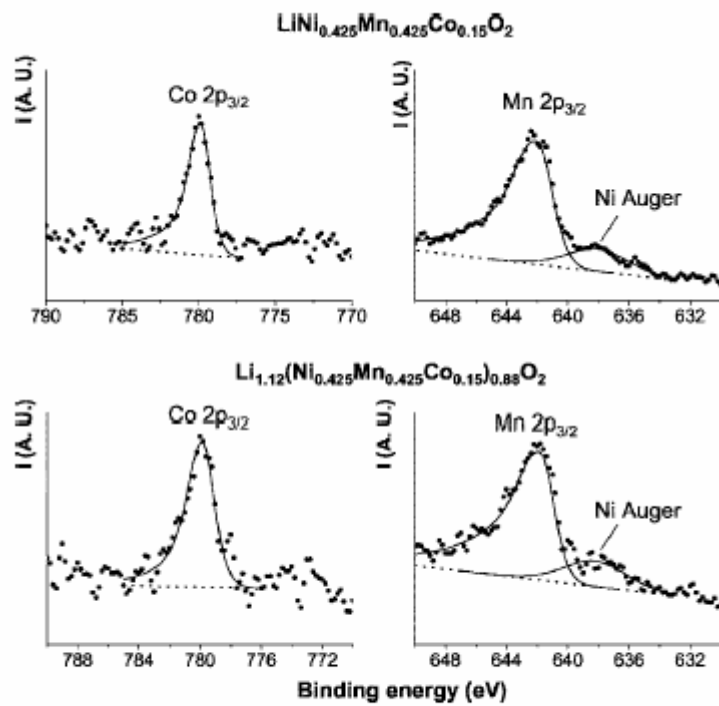


Figure 6. Comparison of the calculated $\text{Co } 2p_{3/2}$ and $\text{Mn } 2p_{3/2}$ XPS spectra (solid line) with the experimental data (points) for $\text{LiNi}_{0.425}\text{Mn}_{0.425}\text{Co}_{0.15}\text{O}_2$ and $\text{Li}_{1.12}(\text{Ni}_{0.425}\text{Mn}_{0.425}\text{Co}_{0.15})_{0.88}\text{O}_2$. Dotted lines represent the background.

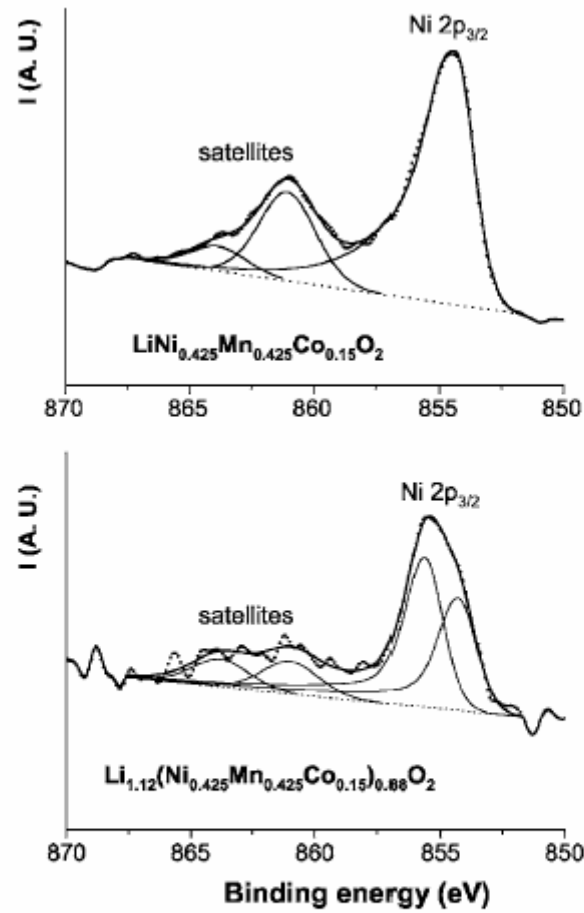


Figure 7. Comparison of the calculated Ni $2p_{3/2}$ XPS spectra (solid line) with the experimental data (points) for $\text{LiNi}_{0.425}\text{Mn}_{0.425}\text{Co}_{0.15}\text{O}_2$ that contains only Ni^{2+} ions and $\text{Li}_{1.12}(\text{Ni}_{0.425}\text{Mn}_{0.425}\text{Co}_{0.15})_{0.88}\text{O}_2$ that contains Ni^{2+} and Ni^{3+} ions. Dotted lines represent the background. For $\text{Li}_{1.12}(\text{Ni}_{0.425}\text{Mn}_{0.425}\text{Co}_{0.15})_{0.88}\text{O}_2$, the Ni $2p_{3/2}$ spectrum was deconvoluted into two contributions.

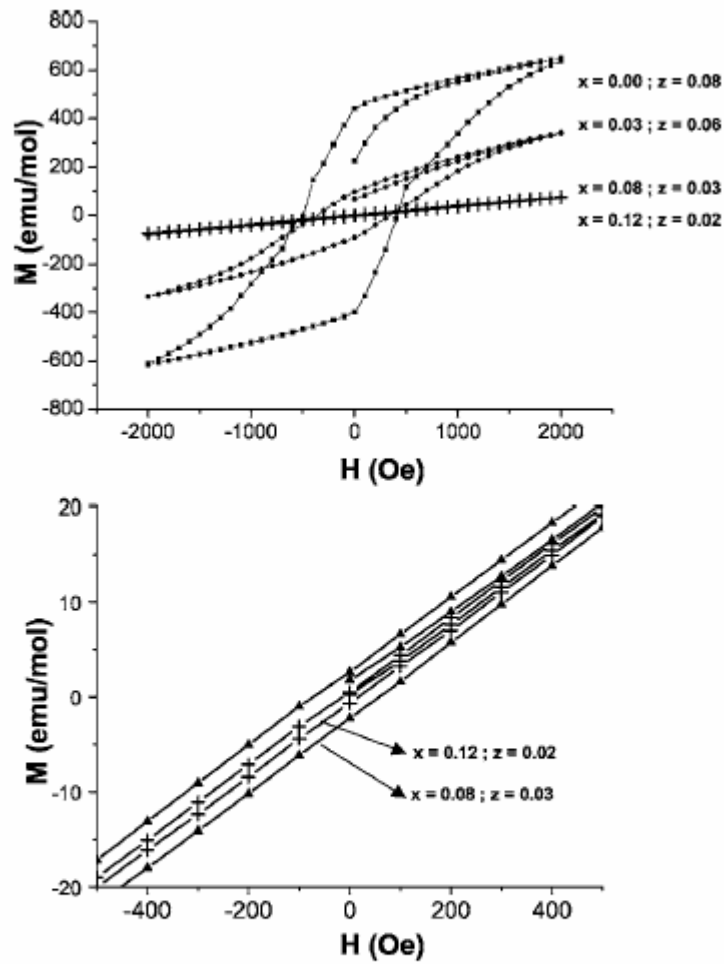


Figure 8. Comparison of the hysteresis loops recorded at 5 K vs magnetic field for the $(\text{Li}_{1-z}\text{Ni}_z)_3\text{b}(\text{Li}_{x+z}\text{Ni}_{0.425(1-x)-z}\text{Mn}_{0.425(1-x)}\text{Co}_{0.15(1-x)})_3\text{aO}_2$ materials ($x = 0, 0.03, 0.08,$ and 0.12). The Ni occupancy (z) in the Li layer was also specified for each material. A zoom of the hysteresis loops recorded for the $x = 0.08$ and 0.12 materials is also given and reveals a decrease of the hysteresis slit for $x = 0.12$.

Table IV. Comparison between the experimental and theoretical Curie constants determined from the Rietveld refinement of the X-ray data of the $\text{Li}_{1+x}(\text{Ni}_{0.425}\text{Mn}_{0.425}\text{Co}_{0.15})_{1-x}\text{O}_2$ materials ($x = 0, 0.03, 0.08,$ and 0.12).

x	$C_{\text{exp.}}$	$C_{\text{th.}}^{\text{a}}$
0.00	1.25	1.22
0.03	1.12	1.08
0.08	1.01	1.02
0.12	0.89	0.92

^a The theoretical Curie-Weiss constants were calculated according to the cationic distributions determined from the refinement of the X-ray data by the Rietveld method.

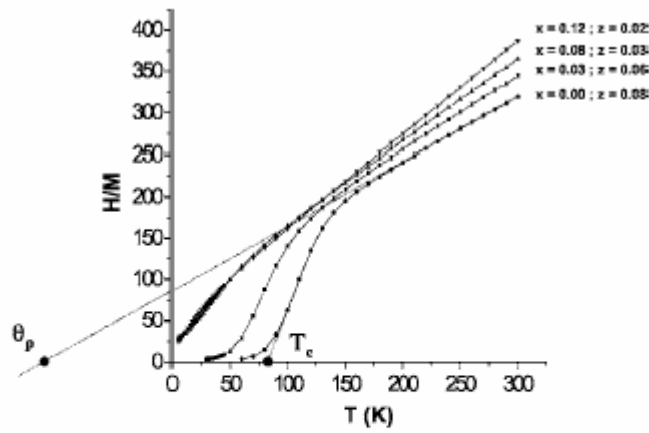


Figure 9. Thermal evolution of the H/M ratio [H the applied field ($H = 10,000$ Oe), M the measured magnetization] for the $(\text{Li}_{1-x}\text{Ni}_x)_{3b}(\text{Li}_{x+z}\text{Ni}_{0.425(1-x)-z}\text{Mn}_{0.425(1-x)}\text{Co}_{0.15(1-x)})_{3a}\text{O}_2$ materials ($x = 0, 0.03, 0.08,$ and 0.12). The Ni occupancy (z) in the Li layer was also specified for each material. The θ_p and T_c temperatures are indicated for the $x = 0$ material.

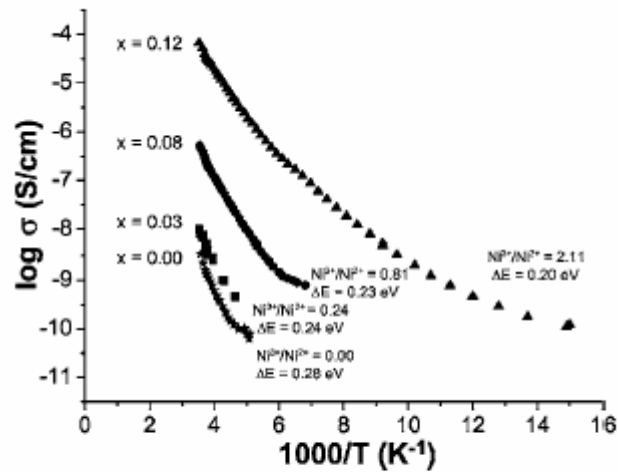


Figure 10. Variation of the logarithm of the electrical conductivity vs reciprocal temperature for the $\text{Li}_{1+x}(\text{Ni}_{0.425}\text{Mn}_{0.425}\text{Co}_{0.15})_{1-x}\text{O}_2$ materials ($x = 0, 0.03, 0.08,$ and 0.12). The $\text{Ni}^{3+}/\text{Ni}^{2+}$ ratio in the slab and the activation energy were specified for each material.

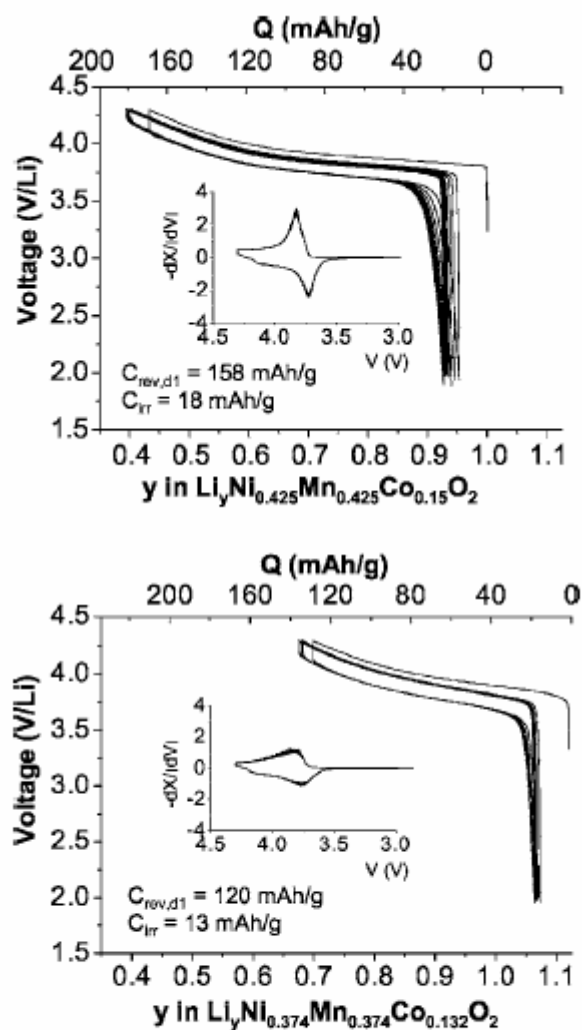


Figure 11. Variation of cell voltage vs lithium amount for the first ten galvanostatic charge/discharge cycles in $\text{Li} \parallel \text{Li}_{1+x}(\text{Ni}_{0.425}\text{Mn}_{0.425}\text{Co}_{0.15})_{1-x}\text{O}_2$ ($x = 0$ and 0.12) at the $C/20$ rate. The first discharge capacity and the irreversible capacity are specified for each cell. The $-dx/dV = f(V)$ incremental capacity curves for the second cycle are also given.

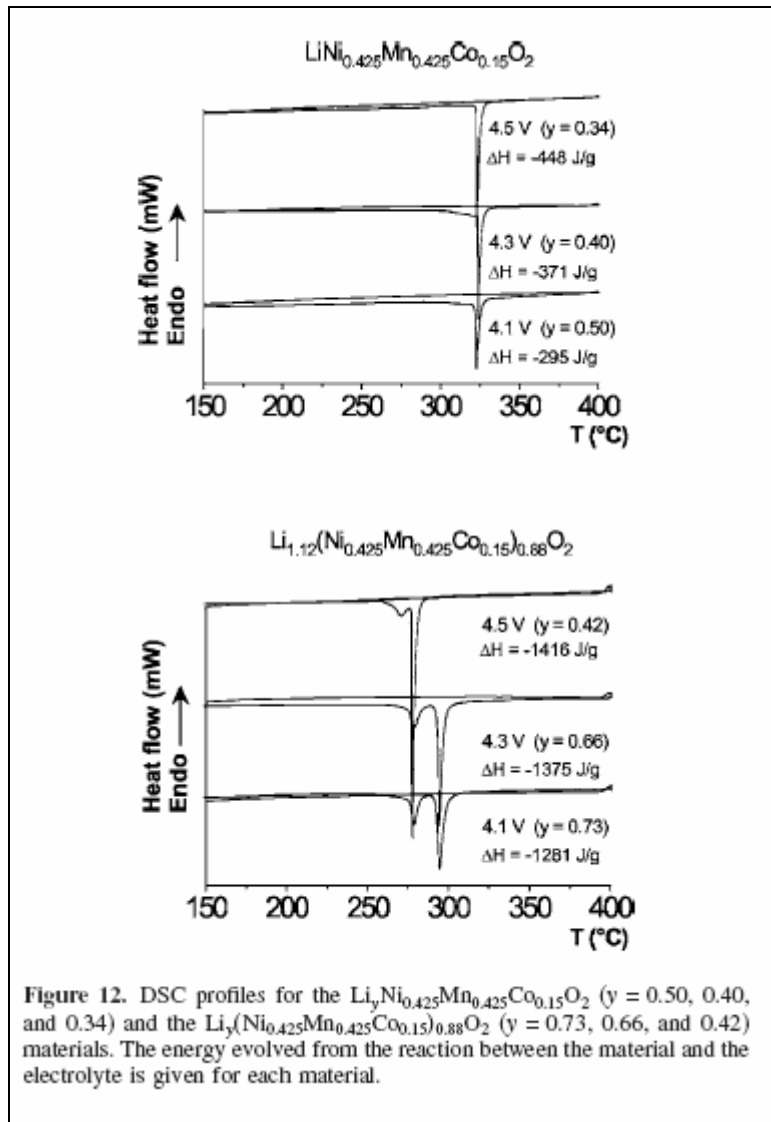


Figure 12. DSC profiles for the $\text{Li}_y\text{Ni}_{0.425}\text{Mn}_{0.425}\text{Co}_{0.15}\text{O}_2$ ($y = 0.50, 0.40,$ and 0.34) and the $\text{Li}_y(\text{Ni}_{0.425}\text{Mn}_{0.425}\text{Co}_{0.15})_{0.88}\text{O}_2$ ($y = 0.73, 0.66,$ and 0.42) materials. The energy evolved from the reaction between the material and the electrolyte is given for each material.

Table V. Cationic distributions and $(\text{Ni}^{4+} + \text{Co}^{4+})/M$ ratio determined for the $\text{Li}_y\text{Ni}_{0.425}\text{Mn}_{0.425}\text{Co}_{0.15}\text{O}_2$ ($y = 0.50, 0.40,$ and 0.34) and $\text{Li}_y(\text{Ni}_{0.425}\text{Mn}_{0.425}\text{Co}_{0.15})_{0.88}\text{O}_2$ ($y = 0.75, 0.66,$ and 0.42) materials.

Pristine material	Cutoff voltage (V)	Cationic distribution	$(\text{Ni}^{4+} + \text{Co}^{4+})/M$ (%)
$(\text{Li}_{0.08}\text{Ni}_{0.08}^{\text{II}})_{3b}(\text{Ni}_{0.345}^{\text{II}}\text{Mn}_{0.425}^{\text{IV}}\text{Co}_{0.15}^{\text{III}}\text{Li}_{0.08})_{3a}$	4.1	$(\text{Li}_{0.50}\text{Ni}_{0.08}^{\text{III}})_{3b}(\text{Ni}_{0.075}^{\text{IV}}\text{Ni}_{0.27}^{\text{III}}\text{Mn}_{0.425}^{\text{IV}}\text{Co}_{0.15}^{\text{III}})_{3a}$	7.5
	4.3	$(\text{Li}_{0.40}\text{Ni}_{0.08}^{\text{III}})_{3b}(\text{Ni}_{0.175}^{\text{IV}}\text{Ni}_{0.17}^{\text{III}}\text{Mn}_{0.425}^{\text{IV}}\text{Co}_{0.15}^{\text{III}})_{3a}$	17.5
	4.5	$(\text{Li}_{0.34}\text{Ni}_{0.08}^{\text{III}})_{3b}(\text{Ni}_{0.235}^{\text{IV}}\text{Ni}_{0.11}^{\text{III}}\text{Mn}_{0.425}^{\text{IV}}\text{Co}_{0.15}^{\text{III}})_{3a}$	23.5
$(\text{Li}_{0.98}\text{Ni}_{0.02}^{\text{II}})_{3b}(\text{Ni}_{0.114}^{\text{II}}\text{Ni}_{0.24}^{\text{III}}\text{Mn}_{0.374}^{\text{IV}}\text{Co}_{0.132}^{\text{III}}\text{Li}_{0.14})_{3a}$	4.1	$(\text{Li}_{0.73}\text{Ni}_{0.02}^{\text{III}})_{3b}(\text{Ni}_{0.256}^{\text{IV}}\text{Ni}_{0.098}^{\text{III}}\text{Mn}_{0.374}^{\text{IV}}\text{Co}_{0.132}^{\text{III}})_{3a}$	29.1
	4.3	$(\text{Li}_{0.66}\text{Ni}_{0.02}^{\text{III}})_{3b}(\text{Ni}_{0.326}^{\text{IV}}\text{Ni}_{0.028}^{\text{III}}\text{Mn}_{0.374}^{\text{IV}}\text{Co}_{0.132}^{\text{III}})_{3a}$	37.0
	4.5	$(\text{Li}_{0.42}\text{Ni}_{0.02}^{\text{III}})_{3b}(\text{Ni}_{0.354}^{\text{IV}}\text{Mn}_{0.374}^{\text{IV}}\text{Co}_{0.132}^{\text{III}})_{3a}$	55.2